LAWRENCE
LIVERMORE
NATIONAL
LABORATORY

LLNL-JRNL-425129

A Computational Study of X-ray Emission from Laser-Irradiated Ge-doped Foams

J. D. Colvin, K. B. Fournier, M. J. May, H. A. Scott

March 5, 2010

Physics of Plasmas

Disclaimer

A Computational Study of X-ray Emission from Laser-Irradiated Ge-doped Foams

Jeffrey D. Colvin, Kevin B. Fournier, Mark J. May and Howard A. Scott

Lawrence Livermore National Laboratory, Livermore, CA 94551

ABSTRACT

New advances in fabrication of low-density high-Z-doped foams have opened new windows on understanding how materials that are not in local thermodynamic equilibrium (LTE) are heated and radiate. In this paper we discuss simulations of the x-ray spectral emissions from laser-irradiated very low-density Ge-doped silica aerogel targets using a 2D radiation-hydrodynamics code incorporating a modern non-LTE super-configuration atomic model. We present the details of the computational model and show that, for the long-scale-length, sub-critical-density, ~2-3 keV electron temperature plasmas created in experiments at the Omega laser facility, the simulations provide a close match to both the measured Ge L-shell emission (~1-1.5 keV) and the measured Ge K-shell emission (~10-11 keV), but only by accounting properly for non-local thermal conduction. The older average-atom atomic model is shown to be inadequate for these non-LTE plasmas.

I. Introduction and Background

It has been known for some time that it may be feasible to create a bright, high-photon-energy x-ray source by heating a low-density target (like a gas or a metal-doped foam target having a density <0.1% of solid density) with a high-power laser.[1] Laser light of wavelength λ_L will propagate through any plasma that has an electron density less than about 1/4 the critical electron density,

$$n_c = 1.1 \times 10^{21}/\lambda_L(\mu m)^2 \text{ cm}^{-3}. \quad (1)$$

For moderate laser intensities (~10^{14} – 10^{16} W cm^{-2}) the laser beam partially ionizes the material via multi-photon photo-ionization, and then, once free electrons are present, the laser deposits its energy along the beam path via inverse bremsstrahlung interactions with these free electrons. At sub-critical densities, the ionization wave and heating wave travels faster than the plasma sonic velocity, as we show below. Thus, the laser beam supersonically and volumetrically heats the low-density material on a time scale shorter than the time scale for the rarefaction wave to decompress and cool the plasma, providing much higher x-ray conversion efficiency (XRCE) in the non-LTE plasma than is obtained by simply irradiating solid targets.[2,3,4] Under-dense high-Z radiators have been confined in the past mainly to high-Z noble gases,[5,6,7] but some efficient x-ray sources have also been created with nano-fiber targets,[8] pre-pulsed metal foils,[9,10] and by irradiating the inside surface of Ti metal-lined cans.[11,12]

The recent development of chemical processes to fabricate high-Z doped aerogel foams[13] has opened access to creating and characterizing bright x-ray sources at other photon energies, particularly bright K-shell emitters in the ~3-13 keV photon energy range (between Ar and Kr). So far, the chemistry has been worked out for doping with Ti, Zn and Ge. In recent years experiments have been carried out on Ti-doped aerogel foams,[14] and on Ge-doped aerogel foams,[15] with comparable numbers of emitting ions as in gas targets.

In the experiments reported by Fournier *et al.*[15], 20 % by number Ge-doped SiO_2 aerogel foams were fabricated inside right-circular cylindrical cans of Be with wall thickness 75 μm. The cans were open at both ends to allow entry of the laser light. Approximately two-dozen such laser targets were made, some small size (1.20 mm length, 1.50 mm ID), some medium size (2.20 mm length, 2.00 mm ID), and some large size (2.20 mm length, 2.50 mm ID), with a few size variants. It is the modeling of these target experiments that we address in this paper.

The targets were heated by 40 beams of the Omega laser[16] located at the University of Rochester Laboratory for Laser Energetics. The Omega laser is a 60-beam Nd-doped glass laser that can deliver up to 30 kJ of 0.351-μm laser light to target chamber center. Because of the beam geometry, we used 40 of the 60 beams, with ~0.5 kJ per beam, for a total of ~20 kJ beam energy onto the target. The beams were arranged in three cones on either side of the can: 10 beams incident at 21.4^o to the can axis, 10 beams incident at 42.0^o to the can axis, and 20 beams incident at 58.8^o to the can axis. All the laser energy was contained in a 1-ns-square pulse (0.2 ns rise to peak power P_m, 1 ns flat top, 0.2 ns fall to zero), with P_m = 2.08 TW in the 21.4^o beams overlapped 0.5 mm in front of each laser entrance hole; P_m = 2.08 TW in the 42.0^o beams overlapped at each laser entrance hole; and P_m = 4.17 TW in the 58.8^o beams overlapped at each laser entrance hole. Each beam produced an elliptical focal spot of rms radius a few hundred microns, but the beam pointing and focal spot size were varied to obtain the trends in x-ray emission with laser intensity.

In addition to size variants, there were also foam-density variants. Full details of the targets, the experiments, the diagnostics, and the experiment results are given in reference 15.

The new research that is reported in this paper is the development of a new super-configuration non-LTE atomic model, its incorporation into a 2D radiation-hydrodynamics computer code, and simulations of the Omega experiments with the more-detailed atomic model. In the next section we discuss the details of the model and its incorporation in a 2D radiation-hydrodynamics computer code. In Section III we present the results of the simulations of one representative Omega shot of one of the typical Ge-doped silica aerogel targets, and discuss how the simulated x-ray emission compares to the measurements and with simulations done with an older average-atom atomic model. Discussion and concluding summary are presented in Section IV.

II. The Model

We use the 2D radiation-hydrodynamics code Lasnex,[17] one of the principal laser-target design tools. The hydrodynamics equations --- conservation of mass, momentum, and energy --- are solved in a Lagrangian formulation (mass is the independent variable). We incorporated into the code a custom-built automatic rezoner based on an equipotential method to keep the mesh lines nearly orthogonal. Rezoning does lead to some numerical diffusion across zone and material boundaries, but this diffusion is negligible everywhere except where the mesh becomes highly distorted at the ends of the Be can at late times, well after the laser has turned off. The hydrodynamics at these locations and at these late times has practically no effect on the heating and x-ray emission of the hot high-Z plasma.

For input of the laser beams, the simulation includes a 3D ray-tracing algorithm adapted for the Omega beam geometry, with absorption by inverse bremsstrahlung. Rays are tracked through the mesh using gradient-index geometrical optics for a fully general set of laser rays originating from random positions on the final focusing lens.

Once the beam energy is deposited along the ray path, this energy is transported from the heated plasma to cooler plasma via thermal conduction and radiation. Both flux-limited plasma electron and ion thermal conductivities are included in the simulation.

For electron conductivities, we use a Spitzer-Harm temperature-gradient-driven formulation,[18] or Lee-More conductivities[19] --- default in the code --- which includes dense plasma effects. The flux limiter can be varied. There is some small sensitivity to the conductivity model and flux limiter, which we discuss in more detail in Section IV. That discussion includes a description of the physical differences between the two conductivity formulations.

In the radiation transport calculation, we use 700 photon energy bins spanning the photon energy range between 5 eV and 29 keV, with the bins distributed so that there is a sufficient number of these energy bins to resolve the L-shell and K-shell structure of all the emitting ions. The equation of state is obtained from the non-LTE calculation.

Ionization states are calculated in non-LTE from either an average-atom model (XSN)[20] or a more detailed super-configuration atomic model (DCA)[21]. In the XSN calculation, an average ionization state is determined for the emitting ion from the screened hydrogenic atomic energy levels, up to 10 levels for the representative atom. The calculation optionally includes correction factors as a mock-up for auto-ionization and di-electronic recombination rates, according to the prescription given by Albritton and Wilson[22].

In the DCA calculation, on the other hand, the rate equations are solved simultaneously to give the population densities of each energy level. The calculation includes about 20 levels for each ionization stage, including doubly excited and auto-ionizing states, with each level corresponding to a super-configuration described by a set of principal quantum number occupations. The maximum principal quantum number included was 10. Energy levels are calculated with screening coefficients and are adjusted to match tabulated ionization energies. Radiative transitions, including $\Delta n=0$ transitions, occur between terms (instead of levels), with tabulated transition energies and oscillator strengths. Line widths include contributions from Doppler, Stark and configuration broadening. Details of this approach are given in Reference 21.

Atomic data are calculated in-line in the new DCA model, and this calculation costs about three times more in computer time than does the XSN calculation to get the non-LTE ionization states. This added cost is small, though, compared to the cost of other stand-alone detailed atomic models. Thus, the big advance here is the development of a detailed non-LTE atomic model that can be affordably incorporated into a radiation-hydrodynamics computer code.

III. Results

For this study we simulated one representative Omega shot (#51167), which put 19.34 kJ of beam energy into one of the medium-size cans (2.20 mm length, 2.00 mm ID) in a 1-ns-square pulse. The can was filled with Ge-doped silica foam with a total density of 4.1 mg cm^{-3}. Foam of this density, when illuminated by the ~19 kJ from the Omega laser, becomes plasma with a nearly uniform electron density of approximately one-tenth the critical density, as shown in Fig. 1. This electron density is ideal for efficient x-ray conversion. This is because the radiated power is proportional to the square of the electron density, so much lower-density plasmas do not radiate as efficiently (and, for a given beam energy, do not get as hot), while plasmas with densities greater than ~$n_c/4$ have plasma waves that anomalously absorb or scatter the incident laser light.

Thus, the Ge-doped aerogel heats supersonically, as illustrated in Fig. 2. Here we show simulated temperature profiles along the can axis at a succession of times between 0.2 ns and 0.8 ns. The heating wave arrives at can center by 0.6 ns. By 0.7 ns the plasma at can center is already hotter than ~1 keV. The ionization/heating front, as seen in Fig. 2, is traveling at a velocity ~1 mm/ns down the axis of the can. This velocity is about a thousand times faster than the sonic velocity in the cold silica, and ~2.5 times the sonic velocity in 2 keV silica plasma. The supersonic heating wave thus heats the plasma relatively uniformly, as shown in Fig. 3. By 0.7 ns the entire volume of the interior of the can is heated to electron temperatures >1 keV (Fig. 3a); by the time the laser turns

off at 1.0 ns, much of the interior volume is heated to electron temperatures >2 keV (Fig. 3b).

The simulations for this shot using the new DCA model closely match the measured *total* Ge L-shell and Ge K-shell emission, as shown in Fig. 4 (i.e., the time-integrated emitted power versus time). In unfolding the measured spectral powers we account for the fact that almost all the low-energy (<1 keV) emission seen by the measuring instrument is coming just from the open can ends, the laser entrance holes. The simulations show that the Be wall transmission is approximately zero for the <1 keV x-rays, and is ~0.05-0.10 for the 1-3 keV x-rays, a spectral interval that contains the Ge L-shell and the Si K-shell emission in the ~1-2 keV spectral interval, but very little emission above ~ 2 keV where the can is more transparent.

Note that XSN under-predicts the total L-shell emission (Fig. 4a) by about 15%. Averaged over six nominally identical shots onto identical targets, the measured total L-shell emission has a standard deviation of 12% from the average. A similar finding has been made recently by other researchers for the 2-3 keV emission from Au-coated spheres (Au M-shell emission) illuminated by 10 kJ of the Omega laser,[23] and for the total emission from the Au coronal blow-off plasma inside vacuum hohlraums illuminated by 150 – 635 kJ of the NIF laser.[24] In both these cases, simulations with XSN under-predicted the measured emission, while simulations with the new DCA model provided a much better fit to the measurements.[21,23-26]

Although the DCA simulations get the total emission correct, the simulated time history is not a particularly good match to the measured time history. The time history from the DCA simulations, however, is a better fit to the measured time history than is the time history from the XSN simulation, both at the lower x-ray energies (Fig. 4a) and at the higher photon energies (Fig. 4b). Note that XSN somewhat over-predicts the total K-shell emission (Fig. 4b), but that is mainly because of the “bump” in emission in the XSN simulation at ~2 ns that appears neither in the DCA simulation nor in the data.

Note also that XSN shows more emission below 3.5 keV at later times (after about 2.5 ns, during the cooling phase of the hot expanding plasma, Fig. 4a) than does either DCA or the measurements.

This is perhaps not surprising, since if there is less energy being radiated away --- as there is at early times in the XSN simulation --- the plasma will cool slower. As seen in Fig. 5, before ~3 ns the on-axis hot spot in the XSN simulation is hotter than the on-axis hot spot in the DCA simulation. Conversely, the plasma in the DCA simulation is emitting more radiation at early times, and is thus radiatively cooling faster. At 2.5 ns, the peak temperature in the plasma is ~0.5 keV cooler in the DCA simulation than in the XSN simulation, and hence this plasma emits less at later times, in better agreement with the data.

The hotter on-axis hot spot in the XSN simulation means the hot spot is at higher pressure, so the energy that is not going into the radiation is instead going in to hydrodynamic motion of the plasma. In the XSN simulation at 2.5 ns, we see more axial motion as the hotter and higher pressure hot spot pushes away the cooler plasma on either side of it, as shown in Fig. 6. The hot spot is located ~1/3 mm inside the LEH, where the axial velocity is zero, and the plasma on either side of this position is moving away from it at a velocity that increases linearly with distance. In the DCA simulation, on the other hand, there is much less axial motion of the plasma interior to the hot spot at 2.5 ns. In the DCA simulation, the greater emission during the heating phase leads to a radiative collapse on axis, much like in astrophysical jets,[27] so the on-axis plasma later in time is not only cooler, but also denser, as shown in Fig. 7.

This finding suggests that, were the DCA model to include more energy levels and more satellite lines, it would increase the emission during the heating phase (early times), and decrease it during the cooling phase (later times), bringing the simulated emitted power history into even better agreement with the data. We tested this supposition with a comparison simulation in which we used a somewhat more detailed

DCA model, one which has a better treatment of the doubly excited states. The more detailed simulation does indeed move the emitted power history in the 0-3.5 keV band into better agreement with data, i.e., more emission at early times, less at late, but only slightly. Peak emitted power is about the same in the more detailed simulation as in the simulation shown in Fig. 4, and peak emitted power still occurs at 1 ns, when the laser first turns off. In the more detailed simulation, however, emitted power at 2 ns is ~13% higher, at 3 ns ~19% lower. Doing the more detailed model, though, does add to the run time: CPU time increased by 60%.

The DCA simulation also captures the principal features of the Ge L-shell and the Si K-shell structure much better than does the XSN simulation, as shown in Fig. 8. The principal Si He-α and Ly-α transitions are clearly resolved in the DCA simulation, Fig. 8a, whereas the Si He-α transition is completely absent in the average-atom XSN simulation, Fig. 8b. Indeed, DCA shows comparable emission in the Si He-α and Ly-α lines, in agreement with spectral measurements, as seen in Fig. 9a. As for the Ge L-shell emission, DCA shows the strongest emission in the Ne-like transitions, whereas XSN puts the strongest emission in the more highly ionized Li-like transitions. The spectral measurements made with a curved crystal spectrometer and shown in Fig. 9a are consistent with stronger emission from the less ionized atoms, although the Ne-like transitions are not seen because the curvature of the crystal is such that these lines miss the film. Additionally, these lines are outside the transmission band-pass of the filters used in the diagnostic, as shown in Fig. 9b.

IV. Discussion and Summary

The principal finding from this work is that the more-detailed DCA non-LTE atomic model provides much better agreement with x-ray emission data than does the older average-atom XSN atomic model. The other significant finding from this work is that there is some small sensitivity of the simulation results to the electron thermal conductivity model and the associated choice of the flux limiter. We get slightly better agreement with data by using Spitzer-Harm electron thermal conductivities with a flux

limiter of f_e=0.2. Using Lee-More conductivities we find that there is no value of the flux limiter that provides a match to the data. Indeed, we find that, using Lee-More conductivities, there is little sensitivity of the emission to the value of the flux limiter. In Fig. 10 we show a comparison of the low-energy (Fig. 10a) and the high-energy (Fig. 10b) emitted powers calculated with the two different electron thermal conductivity models. The DCA atomic model in non-LTE was used in both simulations. Lee-More conductivities with f_e=0.1, the default values in the code for some time now, are used in this comparison because they match older disc and hohlraum data. Note in Fig. 10 that Spitzer-Harm with a larger flux limiter provides a slightly better match to the data at both low and high photon energies.

A more convincing agreement with the data comes from comparing the temperatures simulated with the two different electron thermal conductivity models. As seen in Fig. 11a, the Spitzer-Harm conductivity model gives a peak temperature of 2.64 keV, and the temperature is fairly uniform over a hot spot that is more than 0.5 mm wide. The Lee-More conductivity model, on the other hand, gives a peak temperature of 2.90 keV with a steeper temperature gradient across the hot spot, as seen in Fig. 11b. For this particular shot we inferred a peak temperature of 2.71 keV from a bremsstrahlung fit to the measured continuum spectrum. Averaged over six nominally identical shots onto identical targets, the measured peak electron temperature is $\langle T_e \rangle = 2.73^{\pm}0.12$ keV. Thus, the simulated peak temperature using the Spitzer-Harm model agrees with the measured value to within one standard deviation, while the simulated peak temperature using the Lee-More model does not.

The flux-limited Spitzer-Harm electron thermal flux is given by

$$F_e = \frac{F_{SH} \bullet f_e F_{FS}}{F_{SH} + f_e F_{FS}}, \qquad (2)$$

where

$$F_{SH} = \frac{16\sqrt{2}T_e^{5/2}}{\pi^{3/2}m_e^{1/2}e^4(Z+1)\ln\Lambda}\nabla T_e \quad (3)$$

is the Spitzer-Harm temperature-gradient-driven thermal flux,

$$F_{FS} = \rho n_e m_e^{-1/2} T_e^{3/2} \quad (4)$$

is the free-streaming flux, and f_e is the flux limiter, a variable parameter in our model. The Spitzer-Harm conductivity model assumes full ionization, but even in the absence of full ionization is quite accurate for low-density, high-temperature plasmas[19] like the ones we are considering in this analysis. The Lee-More conductivity model is more accurate at higher densities and lower temperatures, mainly because of how the Coulomb logarithm, $\ln\Lambda$ in eq. 3, is calculated; in the Lee-More model, the Coulomb logarithm, which is a function of the minimum and maximum impact parameters for Coulomb scattering, is formulated to account for the effects of electron degeneracy, screening, and ion coupling, and always has a *minimum* value of 2. This minimum for the Coulomb logarithm translates into a maximum for the conduction flux at a given temperature and density. In the Spitzer-Harm model, on the other hand, the Coulomb logarithm is not constrained to this minimum value. Thus, Lee-More conductivities are somewhat less sensitive to the value of the flux limiter. This is indeed what we find in the simulations.

It has been known for some time that increasing f_e --- i.e., increasing the non-local transport --- flattens the temperature gradient and increases the x-ray emission.[28] We find, however, that no value of f_e provides a good match with the x-ray emissivity data from these laser-driven under-dense radiators using the XSN average-atom model in non-LTE. Using the more-detailed DCA atomic model, however, we do find good agreement with the data. Best agreement is obtained using the Spitzer-Harm model with $f_e = 0.2$.

This is perhaps not surprising, since the supersonic heating of this under-dense plasma results in fairly uniform heating, and thus a relatively shallow temperature gradient in which we can expect non-local heat transport to play a larger role than in the steep temperature gradients in coronal blow-off plasmas.

In summary, we have incorporated a modern DCA non-LTE atomic model into a 2D radiation-hydrodynamics code, and used this model to simulate the x-ray spectral emission from laser-irradiated very low-density Ge-doped silica aerogel foam targets. We find very good agreement between simulated and measured total Ge L-shell and K-shell emission using DCA with a temperature-gradient-driven thermal conductivity model with a flux limiter of 0.2.

The XSN average-atom non-LTE atomic model under-predicts both the Ge L-shell and Si K-shell emission and the total emission integrated over all photon energies. It also cannot reproduce details of the spectral line structure.

Finally, we note that we used this same computational model to design much larger-scale under-dense radiators for the National Ignition Facility laser at the Lawrence Livermore National Laboratory. The first set of shots took place in October and November 2009. We have begun a detailed analysis of the data from these recent shots to provide further benchmarking of the computational model. This work will be the subject of a follow-on paper.

Acknowledgements

The authors owe a debt of gratitude to Stephen Moon of the Lawrence Livermore National Laboratory for initiating this work several years ago. The authors also acknowledge useful and enlightening discussions on all aspects of this work with Stephanie Hansen, currently of Sandia National Laboratories, Albuquerque. This work was performed under the auspices of the US Department of Energy by Lawrence Livermore National Laboratory under contract No. DE-

AC52-07NA27344, with some support received from the US Defense Threat Reduction Agency under the IACRO 09-45501, ``Evaluation of Lasers for X-Ray Production on NIF".

References

1. J. Denavit and D. W. Phillion, "Laser ionization and heating of gas targets for long-scale-length instability experiments", *Phys. Plasmas* **1**, 1971 (1994).
2. C. Constantin, C. A. Back, K. B. Fournier, G. Gregori, O. L. Landen, S. H. Glenzer, E. L. Dewald, and M. C. Miller, "Supersonic propagation of ionization waves in an underdense, laser-produced plasma", *Phys. Plasmas* **12**, 063104 (2005).
3. M. Tanabe, H. Nishimura, S. Fujioka, K. Nagai, A. Iwamae, N. Ohnishi, K. B. Fournier, F. Girard, M. Primout, B. Villette, M. Tobin, and K. Mima, "Supersonic heat wave propagation in laser-produced underdense plasma for efficient x-ray generation", *Proc. Conf. Int. Fusion Sciences and Applications (IFSA2007), J. Phys.: Conf. Series* **112**, 022076 (2008).
4. M. Tanabe, H. Nishimura, N. Ohnishi, K. B. Fournier, S. Fujioka, A. Iwamae, S. B. Hansen, K. Nagai, F. Girard, M. Primout, B. Villette, D. Brebion, and K. Mima, "Characterization of heat-wave propagation through laser-driven Ti-doped underdense plasma", *High Energy Density Phys.* **6**, 89-94 (2010).
5. C. A. Back, J. Grun, C. Decker, L. J. Suter, J. Davis, O. L. Landen, R. Wallace, W. W. Hsing, J. M. Laming, U. Feldman, M. C. Miller, and C. Wuest, "Efficient Multi-keV Underdense Laser-Produced Plasma Radiators", *Phys. Rev. Lett.* **87**, 275003 (2001).
6. C. A. Back, J. Davis, J. Grun, L. J. Suter, O. L. Landen, W. W. Hsing, and M. C. Miller, "Multi-keV x-ray conversion efficiency in laser-produced plasmas", *Phys. Plasmas* **10**, 2047 (2003).
7. K. B. Fournier, C. Constantin, C. A. Back, L. Suter, H.-K. Chung, M. C. Miller, D. H. Froula, G. Gregori, S. H. Glenzer, E. L. Dewald, and O. L. Landen, "Electron-density scaling of conversion efficiency of laser energy into L-shell X-rays", *JQSRT* **99**, 186 (2006).
8. M. Tanabe, H. Nishimura, S. Fujioaka, K. Nagai, M. Yamamoto, Z-Z. Gu, C. Pan, F. Girard, M. Primout, B. Villette, D. Brebion, K. Fournier, A. Fujishima, and K. Mima, "Titanium-dioxide nano-fiber cotton targets for efficient multi-keV x-ray generation", *Appl. Phys. Lett.* **93**, 051505 (2008).
9. F. Girard, J. P. Jadaud, M. Naudy, B. Villette, D. Babonneau, and M. Primout, "Multi-keV x-ray conversion efficiencies of laser pre-exploded titanium foils", *Phys. Plasmas* **12**, 092705 (2005).
10. D. Babonneau, M. Primout, F. Girard, J.-P. Jadaud, M. Naudy, B. Villette, S. Depierreux, C. Blancard, G. Faussurier, K. B. Fournier, L. Suter, R. Kauffman, S. Glenzer, M. C. Miller, J. Grun, and J. Davis, "Efficient multi-keV x-ray sources from laser-exploded metallic thin foils", *Phys. Plasmas* **15**, 092702 (2008).
11. M. Primout, L. Jacquet, D. Babonneau, F. Girard, B. Villette, J.-P. Jadaud, M. Naudy, Ph. Stemmler, and J. L. Ulmer, "Recent progress in metal-lined cylindrical hohlraums as efficient x-ray sources", *J. Phys.: Conf. Ser.* **112**, 042051 (2008).

12. F. Girard, M. Primout, B. Villette, Ph. Stemmler, L. Jacquet, D. Babonneau, and K. B. Fournier, "Titanium and germanium lined holraums and halfraums as multi-keV x-ray radiators", *Phys. Plasmas* **16**, 052704 (2009).
13. B. J. Clapsaddle, D. W. Sprehn, A. E. Gash, J. H. Satcher, Jr., and R. L. Simpson, "A versatile sol-gel synthesis route to metal-oxide nanocomposites that contain metal oxides as the major phase", *J. Non-Crystalline Solids* **350**, 173 (2004).
14. K. B. Fournier, C. Constantin, J. Poco, M. C. Miller, C. A. Back, L. J. Suter, J. Satcher, J. Davis, and J. Grun, "Efficient Multi-keV X-ray Sources from Ti-Doped Aerogel Targets", *Phys. Rev. Lett.* **92**, 165005 (2004).
15. K. B. Fournier, J. H. Satcher, M. J. May, J. F. Poco, C. M. Sorce, J. D. Colvin, S. B. Hansen, S. A. MacLaren, S. J. Moon, J. F. Davis, F. Girard, B. Villette, M. Primout, D. Babonneau, C. A. Coverdale, and D. E. Beutler, "Absolute x-ray yields from laser-irradiated germanium-doped low-density aerogels", *Phys. Plasmas* **16**, 052703 (2009).
16. T. R. Boehly, D. L. Brown, R. S. Craxton, R. L. Keck, J. P. Knauer, J. H. Kelly, T. J. Kessler, S. A. Kumpan, S. J. Loucks, S. A. Letzring, F. J. Marshall, R. L. McCrory, S. F. B. Morse, W. Seka, J. M. Soures, and C. P. Verdon, *Opt. Commun.* **133**, 495 (1997).
17. G. B. Zimmerman and W. L. Kruer, "Numerical Simulation of Laser-Initiated Fusion", *Comments Plasma Phys. Control. Fusion* **2**, 51 (1975).
18. L. Spitzer, *Physics of Fully Ionized Gases* (Wiley, New York, N. Y., 1962).
19. Y. T. Lee and R. M. More, "An electron conductivity model for dense plasmas", *Phys. Fluids* **27**, 1273 (1984).
20. W. A. Lokke and W. Grasberger, LLNL Report No. UCRL 52276 (Lawrence Livermore National Laboratory, Livermore, CA, 1977).
21. H. A. Scott and S. B. Hansen, "Advances in NLTE Modeling for Integrated Simulations", *High Energy Density Phys.* **6**, 39-47 (2010).
22. J. R. Albritton and B. G. Wilson, "NLTE ionization and energy balance in high-Z laser-plasmas including two-electron transitions", *JQSRT* **65**, 1-13 (2000).
23. E. L. Dewald, M. Rosen, S. H. Glenzer, L. J. Suter, F. Girard, J.-P. Jadaud, J. Schein, C. Constantin, F. Wagon, G. Huser, P. Neumayer, and O. L. Landen, "X-ray conversion efficiency of high-Z hohlraum wall materials for indirect drive ignition", *Phys. Plasmas* **15**, 072706 (2008).
24. R. E. Olsen, L. J. Suter, J. L. Kline, D. A. Callahan, M. D. Rosen, K. Widmann, E. A. Williams, D. E. Hinkel, N. B. Meezan, G. A. Rochau, A. L. Warrick, S. H. Langer, C. Thomas, S. N. Dixit, E. L. Dewald, M. B. Schneider, J. D. Moody, P. Michel, R. J. Wallace, O. L. Landen, J. Edwards, B. J. MacGowan, and S. H. Glenzer, "Lasnex simulations of NIF vacuum hohlraum commissioning experiments", in *Proc. Conf. Int. Fusion Sciences and Applications (IFSA2009), J. Phys.: Conf. Series*, in press (2010).
25. L. Suter, S. Hansen, M. Rosen, P. Springer, and S. Haan, "Effect of NLTE Emissivity Models on NIF Ignition Hohlraum Power Requirements", in *Proc. 16th Int. Conf. on Atomic Processes in Plasmas* (Monterey, CA, March 22-26, 2009), *AIP Conf. Proc.* **1161**, 3 (Melville, N. Y., 2009).
26. M. Rosen, H. Scott, L. Suter, and S. Hansen, "Improvements in Modeling Au Sphere Non-LTE X-ray Emission", *Bull. A.P.S.* **53**, 36 (2008).
27. A. B. Reighard, R. P. Drake, K. K. Dannenberg, D. J. Kremer, M. Grosskopf, S. G. Glendinning, T. S. Perry, B. A. Remington, J. Greenough, J. Knauer, T. Boehly, S. Bouquet,

L. Boireau, M. Koenig, and T. Vinci, "Observation of collapsing radiative shocks in laboratory experiments", *Phys. Plasmas* **13**, 082901 (2006).

28. G. Wang and T. Chang, "Laser X-ray Conversion and Electron Thermal Conductivity", *Plasma Science & Tech*. **3**, 653 (2001).

Figure Captions

Fig. 1. Simulated electron density contours at 0.6 ns for the target of Omega shot #51167. The closed red curve shows the outline of the Be can that contains the Ge-doped silica plasma. Only one quadrant is shown; the contours have rotational symmetry around the can axis (radial coordinate r=0) and reflection symmetry in the mid-plane (the plane at z=0). The laser beams enter from the right.

Fig. 2. Profiles of electron temperature along the can axis at times ranging from 0.2 ns (right-most black curve) to 0.8 ns (left-most blue curve) in steps of 0.1 ns.

Fig. 3. Electron temperature contours at a) 0.7 ns and b) 1.0 ns as simulated with the DCA non-LTE atomic model and Spitzer-Harm electron thermal conductivities. The closed red curve shows the outline of the Be can that contains the Ge-doped silica plasma. Only one quadrant is shown; the contours have rotational symmetry around the can axis (radial coordinate r=0) and reflection symmetry in the mid-plane (the plane at z=0). The laser beams enter from the right.

Fig. 4. X-ray emitted power as a function of time in a) photon energies of 0-3.5 keV and b) photon energies of 9-11 keV as measured on Omega shot #51167 (black curves), as simulated with the DCA non-LTE atomic model (blue curves), and as simulated with the XSN non-LTE atomic model (red curves).

Fig. 5. Maximum electron temperature on axis as a function of time, as simulated with the DCA non-LTE atomic model (blue curve), and as simulated with the XSN non-LTE atomic model (red curve).

Fig. 6. Profile of the axial component of plasma velocity along the can axis at 2.5 ns, as simulated with the DCA non-LTE atomic model (blue curve), and as simulated with the

XSN non-LTE atomic model (red curve). Positive velocities are out (away from can center, which is at axial coordinate z=0)), negative are in (toward can center).

Fig. 7. Maximum density on axis as a function of time, as simulated with the DCA non-LTE atomic model (blue curve), and as simulated with the XSN non-LTE atomic model (red curve)

Fig. 8. Accumulated x-ray emitted spectral energy as a function of photon energy at four times, a) as simulated with the DCA non-LTE atomic model, and b) as simulated with the XSN non-LTE atomic model.

Fig. 9. a) X-ray spectra from Omega shot #39152 (somewhat less energy into a smaller can than in shot #51167) as measured with the HENWAY crystal spectrometer (see Ref. 15). b) Filter transmission as a function of photon energy for the HENWAY channel that recorded the Si K-shell and Ge L-shell emission, with the positions of the principal Si and Ge transitions indicated.

Fig. 10. X-ray emitted power as a function of time in a) photon energies of 0-3.5 keV and b) photon energies of 9-11 keV as measured on Omega shot #51167 (black curves), as simulated with the DCA non-LTE atomic model and Spitzer-Harm electron thermal conductivities (blue curves), and as simulated with the DCA non-LTE atomic model and Lee-More electron thermal conductivities (red curves).

Fig. 11. Electron temperature contours at 0.6 ns, a) as simulated with the DCA non-LTE atomic model and Spitzer-Harm electron thermal conductivities, and b) as simulated with the DCA non-LTE atomic model and Lee-More electron thermal conductivities. The closed red curve shows the outline of the Be can that contains the Ge-doped silica plasma. Only one quadrant is shown; the contours have rotational symmetry around the can axis (radial coordinate r=0) and reflection symmetry in the mid-plane (the plane at z=0). The laser beams enter from the right.

Colvin_Fig.1

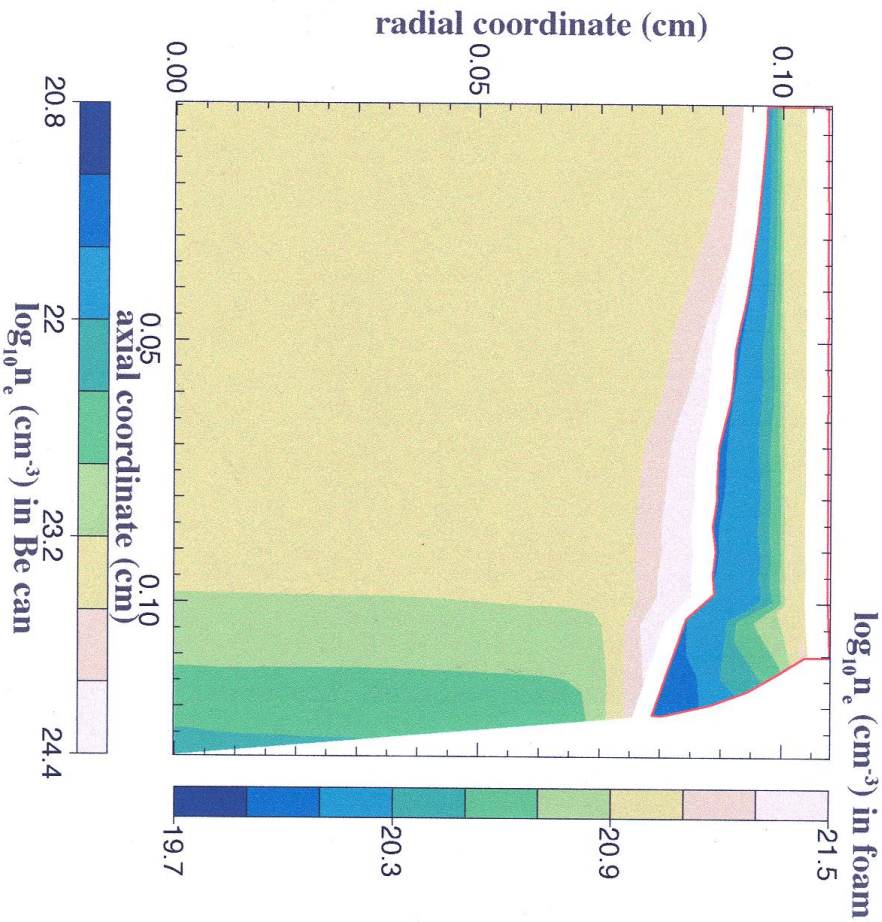
radial coordinate (cm)
0.00
0.05
0.10
axial coordinate (cm)
0.05
0.10
log10ne (cm-3) in foam
19.7
20.3
20.9
21.5
log10ne (cm-3) in Be can
20.8
22
23.2
24.4

Colvin_Fig.2

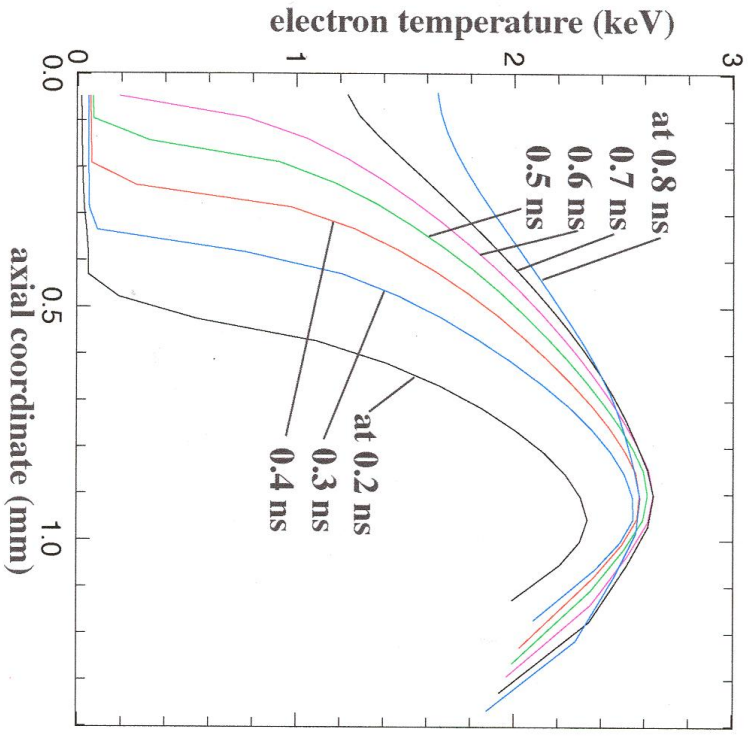
electron temperature (keV)
0
1
2
3
0.0
0.5
1.0
axial coordinate (mm)
at 0.8 ns
0.7 ns
0.6 ns
0.5 ns
at 0.2 ns
0.3 ns
0.4 ns

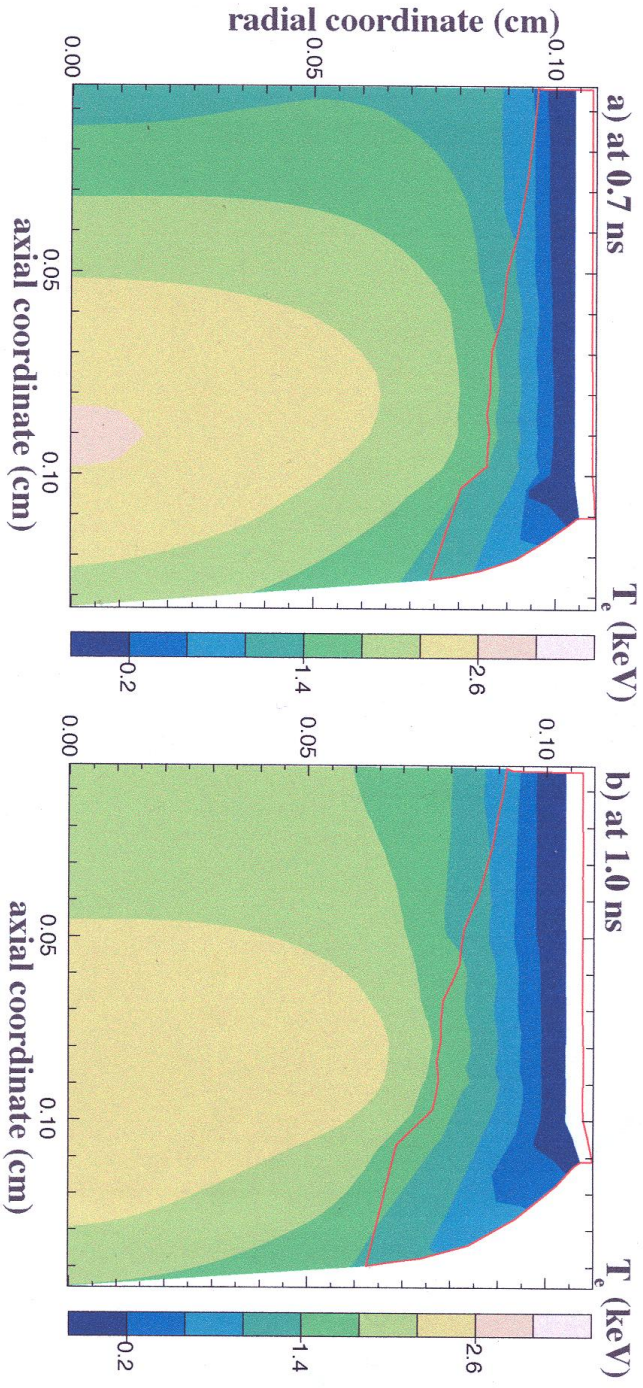
radial coordinate (cm)
0.00
0.05
0.10
a) at 0.7 ns
axial coordinate (cm)
0.05
0.10
T_e (keV)
0.2
1.4
2.6
b) at 1.0 ns

Colvin_Fig.3

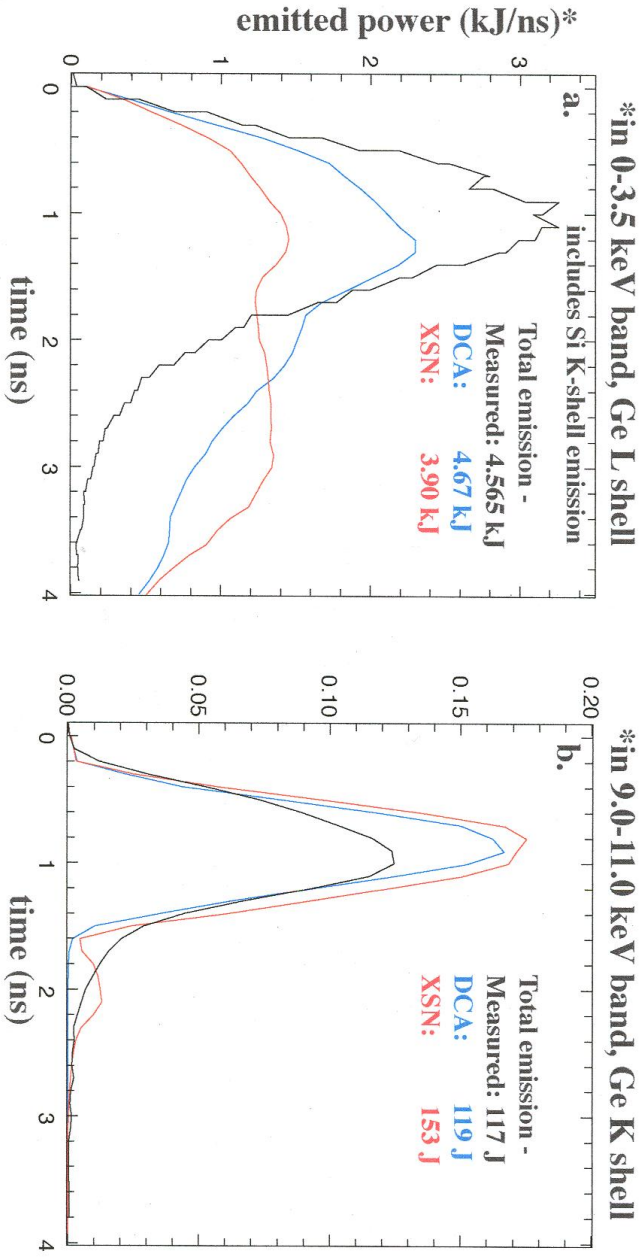
emitted power (kJ/ns)*
a.
*in 0-3.5 keV band, Ge L shell
includes Si K-shell emission
Total emission -
Measured: 4.565 kJ
DCA: 4.67 kJ
XSN: 3.90 kJ
time (ns)
b.
*in 9.0-11.0 keV band, Ge K shell
Total emission -
Measured: 117 J
DCA: 119 J
XSN: 153 J
time (ns)

Colvin_Fig.4

Colvin_Fig.5

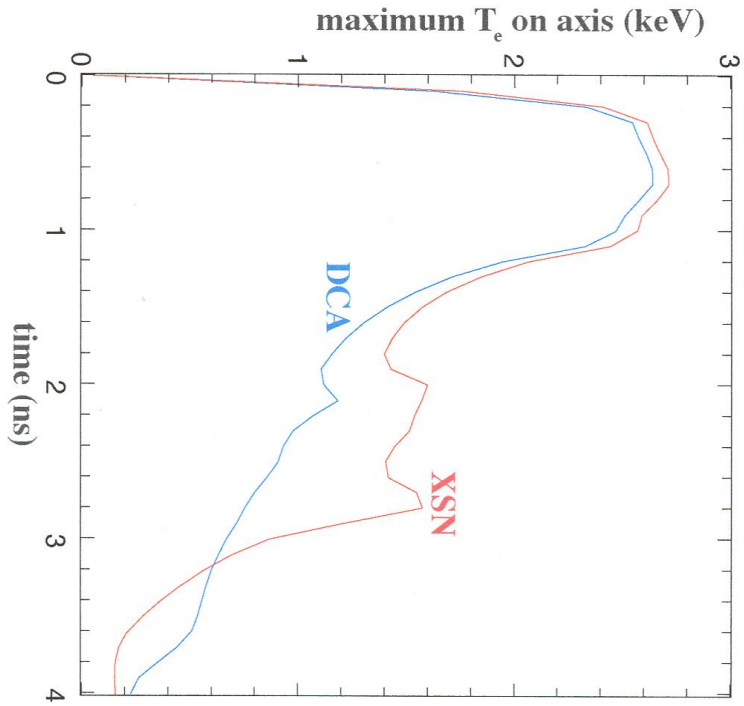

Colvin_Fig.6

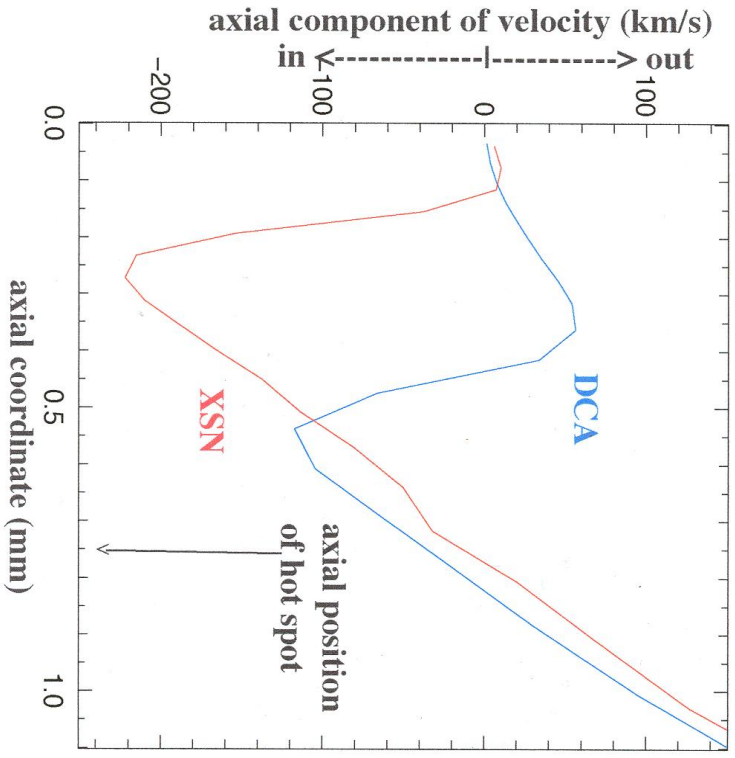
axial component of velocity (km/s)
in <----------|----------> out
−200
−100
0
100
0.0
0.5
1.0
axial coordinate (mm)
DCA
XSN
axial position
of hot spot

Colvin_Fig.7

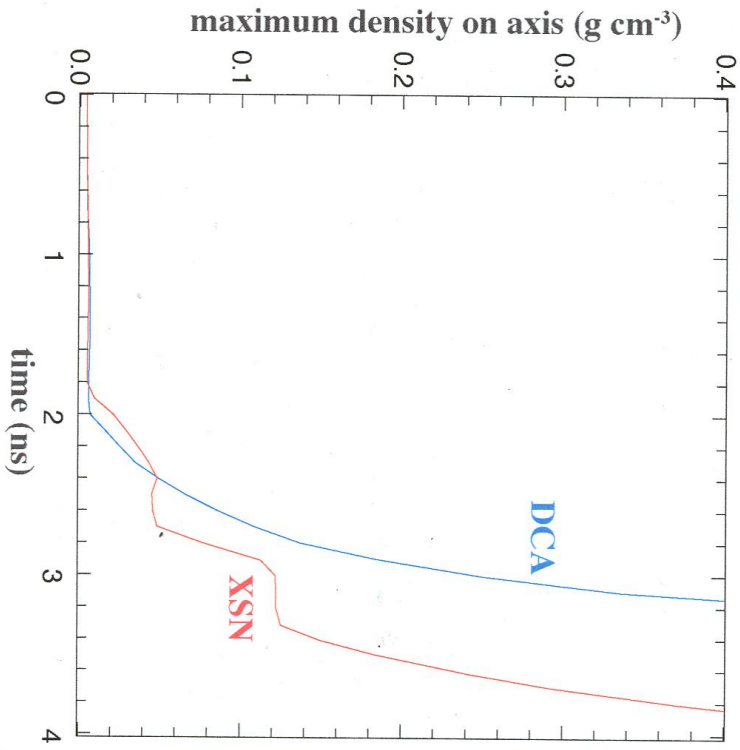
maximum density on axis (g cm-3)
0.0
0.1
0.2
0.3
0.4
0
1
2
3
4
time (ns)
DCA
XSN

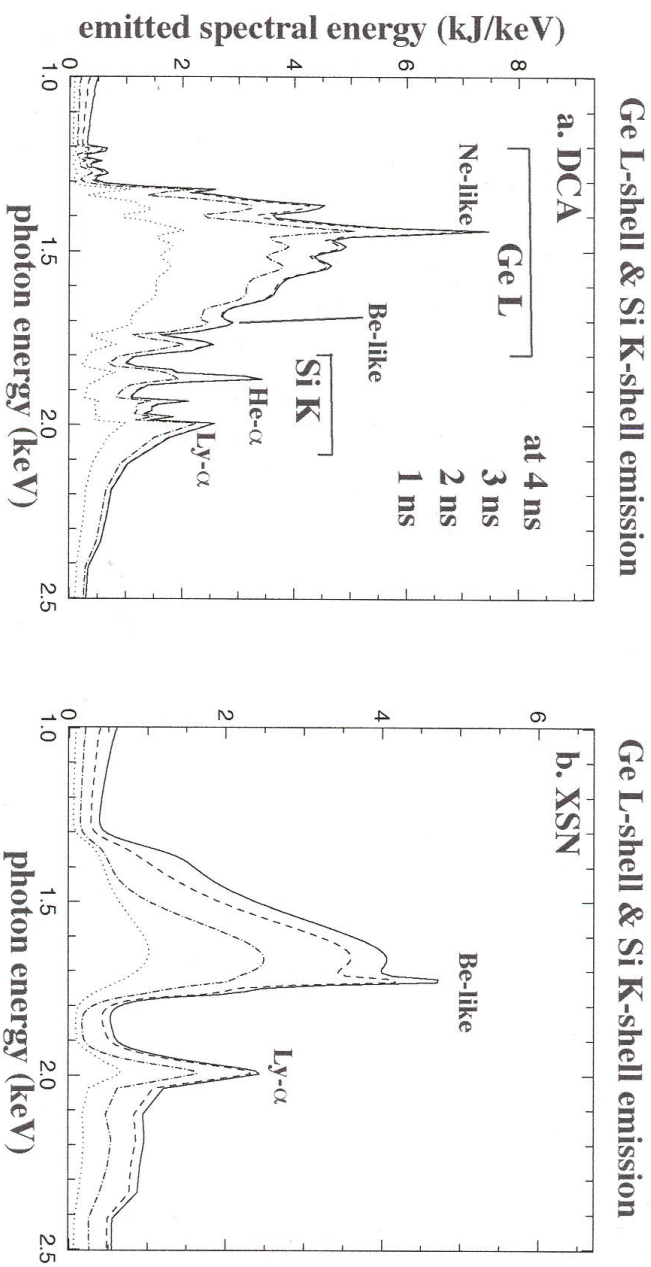
Ge L-shell & Si K-shell emission
a. DCA
emitted spectral energy (kJ/keV)
Ge L
Ne-like
Be-like
Si K
He-α
Ly-α
at 4 ns
3 ns
2 ns
1 ns
photon energy (keV)
Ge L-shell & Si K-shell emission
b. XSN
Be-like
Ly-α
photon energy (keV)

Colvin_Fig.8

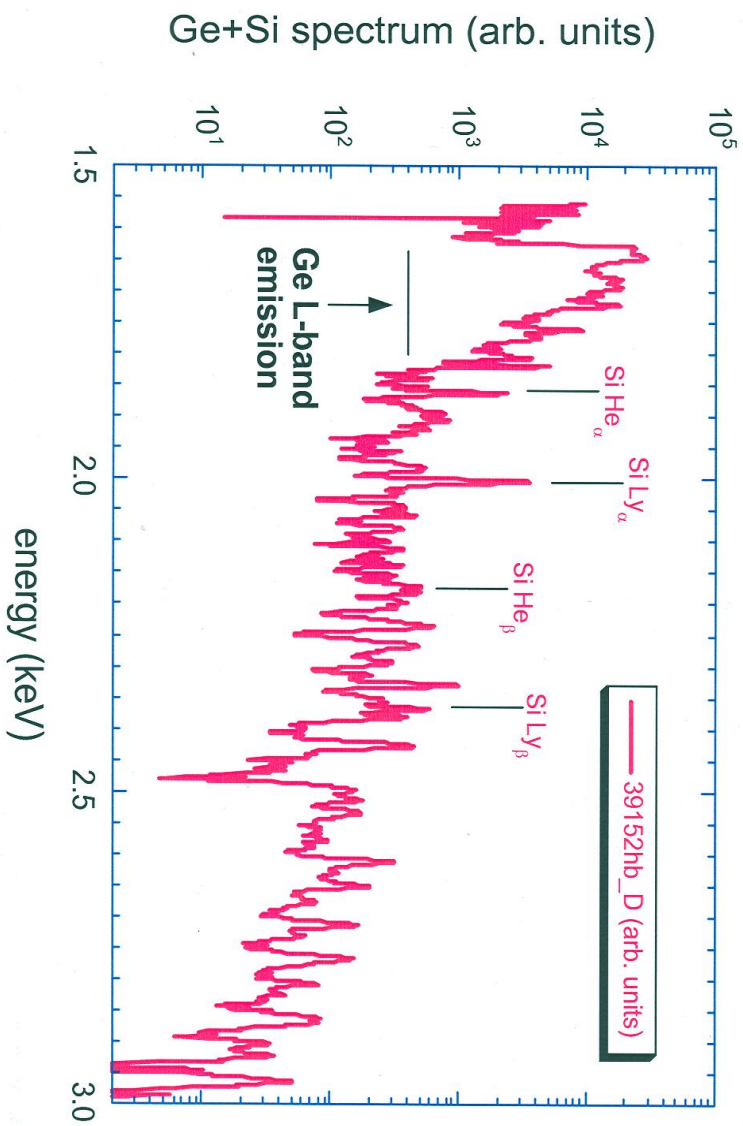

Colvin_Fig.9a

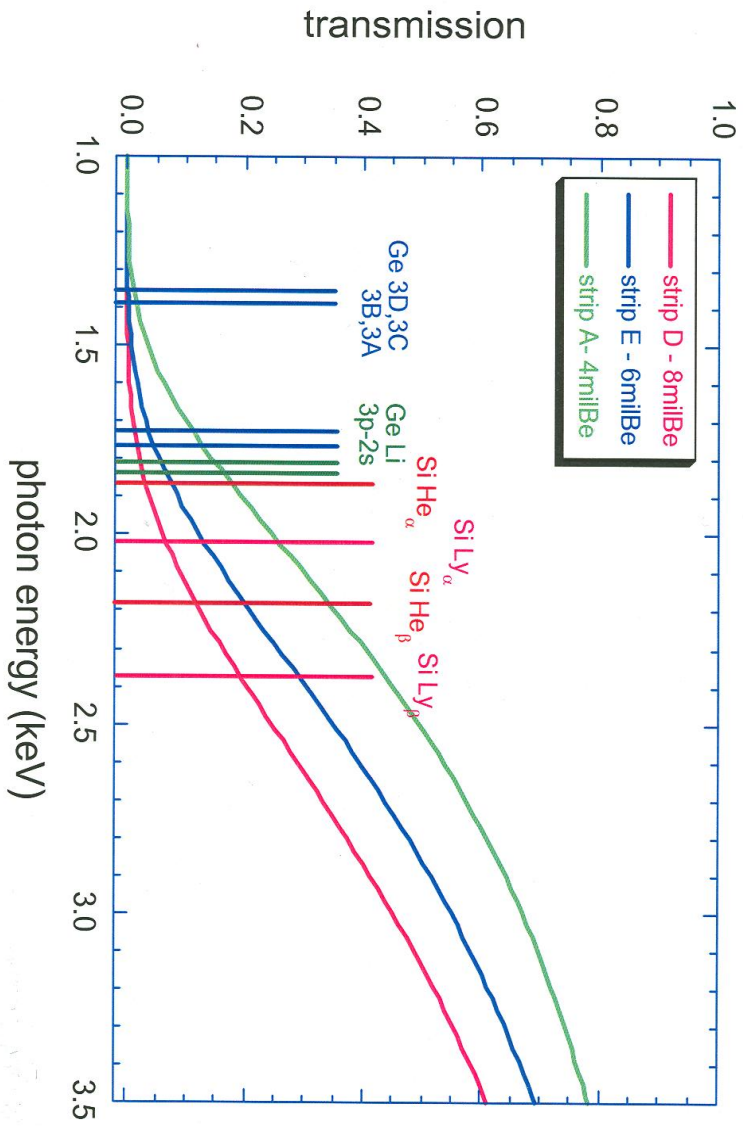

Colvin_Fig.9b

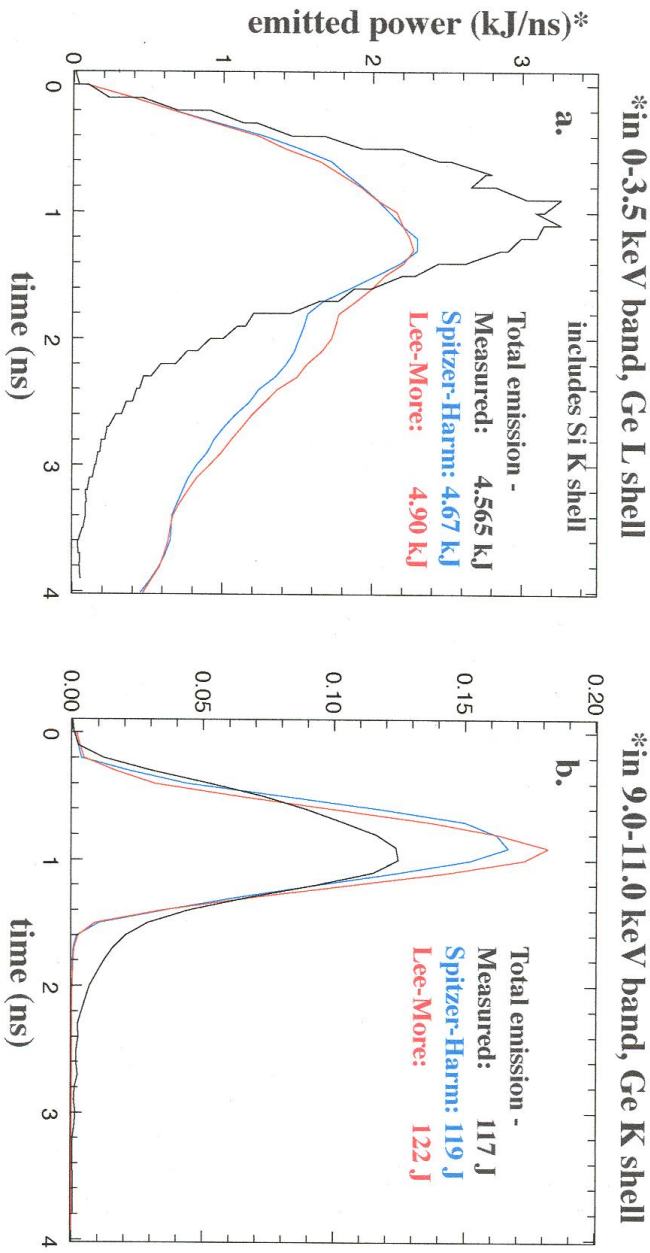

Colvin_Fig.10

Colvin_Fig.11